New constraints on metamorphism in the Highjump Archipelago, East Antarctica

NAOMI M. TUCKER and MARTIN HAND

Department of Earth Science, School of Physical Sciences, The University of Adelaide, Adelaide, SA 5005, Australia
naomi.tucker@adelaide.edu.au

Abstract: The age and conditions of metamorphism in the Highjump Archipelago, East Antarctica, are investigated using samples collected during the 1986 Australian Antarctic expedition to the Bunger Hills–Denman Glacier region. *In situ* U-Pb dating of monazite from three metasedimentary rocks yields ages between *c.* 1240–1150 Ma and a weighted mean $^{207}Pb/^{206}Pb$ age of 1183 ± 8 Ma, consistent with previous constraints on the timing of metamorphism in this region and Stage 2 of the Albany–Fraser Orogeny in south-western Australia. This age is interpreted to date the development of garnet ± sillimanite ± rutile-bearing assemblages that formed at *c.* 850–950°C and 6–9 kbar. Peak granulite facies metamorphism was followed by decompression, evidenced largely by the partial replacement of garnet by cordierite. These new pressure–temperature determinations suggest that the Highjump Archipelago attained slightly higher temperature and pressure conditions than previously proposed and that the rocks probably experienced a clockwise pressure–temperature evolution.

Introduction

The correlation of Rodinian crustal domains relies upon a thorough knowledge of the tectonothermal history of those vestiges that are preserved in the present day continents. The Bunger Hills and Highjump Archipelago (HJA), together with the Windmill Islands, comprise one of a few outcrops of the East Antarctic Craton in Wilkes Land, East Antarctica, and the only exposure that can be directly correlated with the Musgrave–Albany–Fraser Orogen (MAFO), which is the Australian equivalent in Rodinian supercontinent reconstructions (Fig. 1; Clarke *et al.* 1995, Harris 1995, Nelson *et al.* 1995, Clark *et al.* 2000, Fitzsimons 2000, 2003, Duebendorfer 2002, Aitken & Betts 2008, Boger 2011). Furthermore, the Bunger Hills and HJA occupy a focal position at the very western periphery of this system.

Intercontinental stitching points are invoked between the MAFO and the Bunger Hills–HJA region on the basis of Gondwanan reconstructions (e.g. White *et al.* 2013 and references therein) that juxtapose these two continents as well as apparent similarities in the timing of metamorphism, magmatism and deformation. However, the precise configuration of the Australian plate is a source of controversy between the various tectonic reconstructions. Furthermore, the HJA and Bunger Hills are located within a region of disputed overlap between the different suggested fits and close to a critical piercing point. While the Australian part of the MAFO has been intensely studied (e.g. Clark *et al.* 2000,

Kirkland *et al.* 2011, 2013, 2015, Smithies *et al.* 2011, 2015, Smits *et al.* 2014, Spaggiari & Tyler 2014, Howard *et al.* 2015, Spaggiari *et al.* 2015, Tucker *et al.* 2015, Walsh *et al.* 2015), prior geological knowledge on the Bunger Hills and HJA is very limited with interpretations based on few reconnaissance geochronological and metamorphic studies.

This study uses *in situ* U-Pb monazite geochronology and quantitative phase equilibria modelling to place new constraints on the metamorphic evolution of the largely undescribed HJA. We utilize thin sections from samples collected during the 1986 Australian Antarctic expedition to the Bunger Hills, Obruchev Hills and Denman Glacier region (Sheraton *et al.* 1995). The geographical remoteness and thus logistical challenges in accessing the HJA means that legacy samples provide one of the few enduring records of the original rock characteristics. Nevertheless, these samples yield substantial and useful information regarding the timing and pressure–temperature (P–T) conditions of metamorphism in the HJA.

Geological setting

The HJA comprise a narrow belt of small, exposed rocky islands situated north of the Bunger Hills in East Antarctica (~100°E, 66°S; Fig. 1). The HJA spans ~93 km, varies from 9–23 km in width and extends north-eastwards from the Taylor Islands to the Southern Ocean. Few studies document this region with previous geological
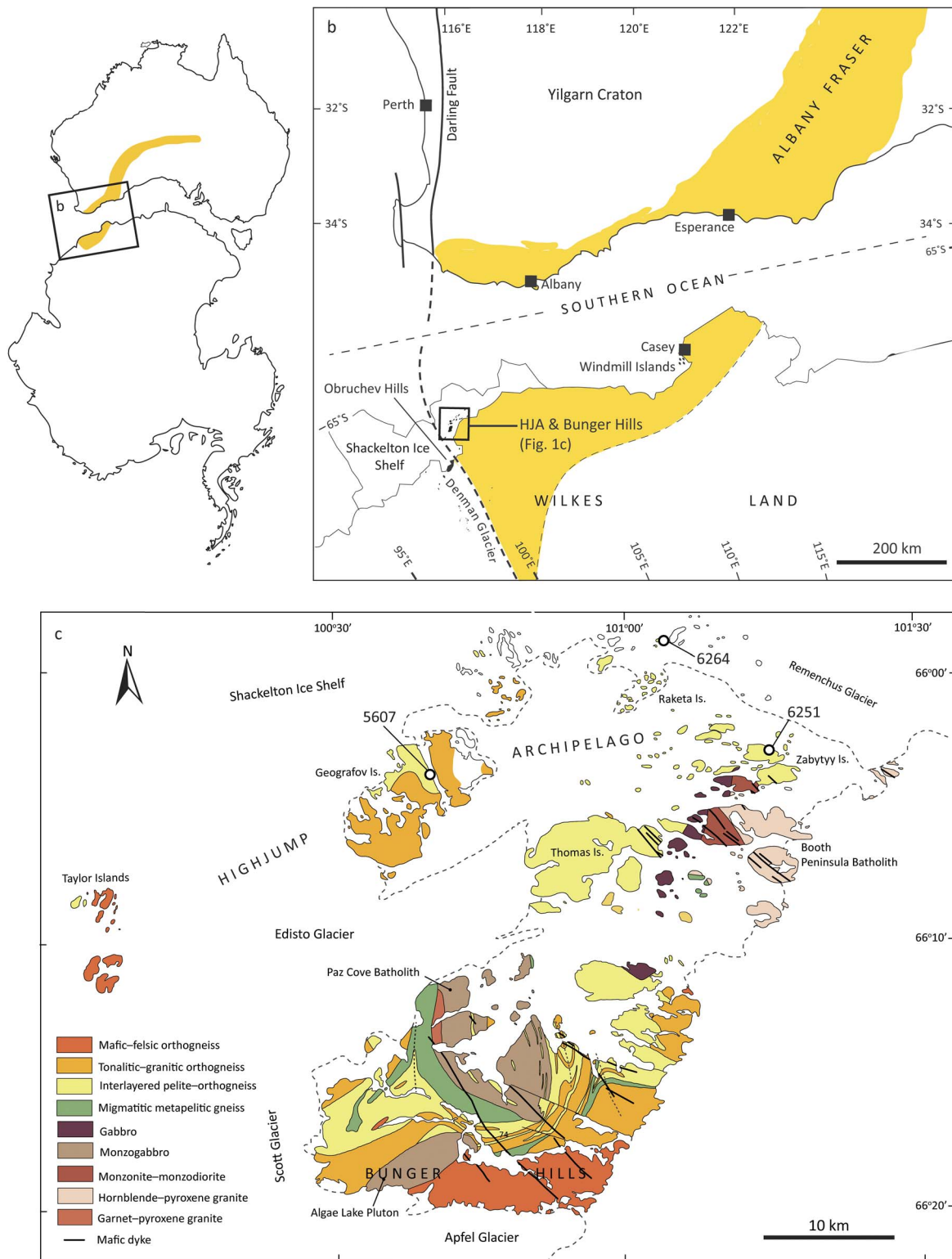
Fig. 1. Location of the Bunger Hills and Highjump Archipelago (HJA) in Wilkes Land, East Antarctica. **a.** The approximate location of the Musgrave–Albany–Fraser Orogen in Australia and Antarctic. The position of the two continents reflects their relative positioning in Gondwanan reconstructions. **b.** Wilkes Land coastline between Casey and Mirny stations showing the approximate location of the Bunger Hills, Obruchev Hills and Windmill Islands (figure modified from Boger 2011). The location of b. is represented by the boxed region on the map of Australia and Antarctica in a. **c.** Simplified regional geology of the Bunger Hills and HJA. The location of samples used in this study are indicated (modified from Sheraton *et al.* 1995).

Table I. Summary of samples.

Sample	UTM (Zone 47D)		Geographical location	Inferred peak mineralogy	Age (Ma)	Peak P–T
	Easting	Northing				
8628-6264	593859	2680326	North Raketa Island	g–sill–ilm–ru–pl–ksp–liq–q	1188 ± 12	$> 900°C, > 7\,kbar$
8628-5607	576132	2671600	Geografov/Currituck Island	g–sill–ilm–ru–pl–liq–q	1161 ± 18	$850–950°C, 8–10\,kbar$
8628-6251	601996	2672796	Zabyyty Island	g–cd–ilm–pl–ksp–liq–q	1186 ± 11	$850–950°C, 5.4–6.6\,kbar$

Mineral abbreviations from Holland & Powell (1998).

investigations based on only two Antarctic expeditions (1956–57 and 1986), as primarily recorded by Ravich *et al.* (1968) and Sheraton *et al.* (1995).

The rocks of the Bunger Hills and HJA consist of predominantly tonalitic–granitic orthogneiss with lesser mafic granulite, interlayered orthogneiss–pelite and migmatitic garnet–sillimanite–cordierite-bearing metasedimentary rocks (Sheraton *et al.* 1993, 1995). Sheraton *et al.* (1992) date the age of the igneous protoliths to felsic orthogneiss from the south-western Bunger Hills and Thomas Island to 1699 ± 15 and 1521 ± 29 Ma, respectively. Tonalitic orthogneiss from the Obruchev Hills, south-west of the Bunger Hills, is dated to the late Archean (*c.* 2640 Ma; Sheraton *et al.* 1992). Within the Bunger Hills, three large intrusive bodies, the Paz Cove batholith, the Algae Lake pluton and the Booth Peninsula batholith, also crop out (Sheraton *et al.* 1992, 1993, 1995). These voluminous plutonic rocks comprise gabbro, monzogabbro, monzodiorite and granite, and were emplaced between *c.* 1170–1150 (Sheraton *et al.* 1992). Dolerite dykes were emplaced at *c.* 1140 Ma, involving at least four chemically distinct suites, and alkaline mafic dykes intruded at *c.* 500 Ma (Sheraton *et al.* 1990).

The definitive structural history of the Bunger Hills–HJA region is debated; however, it is considered to have undergone at least three deformation events (Stüwe & Wilson 1990, Ding & James 1991, Sheraton *et al.* 1993, 1995, Harris 1995). The earliest recognized event is characterized by a layer-parallel S1 gneissic fabric (Sheraton *et al.* 1992) ascribed to crustal extension (Stüwe & Wilson 1990). D2 is characterized by pervasive, tight to isoclinal and asymmetric F2 folding (Ding & James 1991, Sheraton *et al.* 1992) interpreted to reflect compression (Stüwe & Wilson 1990). D2 structures were reoriented during regional scale D3 open and upright folding (Ding & James 1991, Sheraton *et al.* 1992). The age of emplacement of the major plutonic bodies relative to deformation is the main source of contention. Though generally, intrusion of the Paz Cove batholith and Algae Lake pluton are considered synchronous with the last major stage of deformation (Ding & James 1991, Sheraton *et al.* 1992). The Booth Peninsula batholith cross cuts D3 structures and is thus considered to have intruded post-D3 tectonism (Sheraton *et al.* 1992). Subsequent, localized formation of shear

zones, some coeval with mafic dyke emplacement, is also proposed (Sheraton *et al.* 1992).

Previous studies utilizing conventional geothermobarometry estimated that peak metamorphic conditions were ~750–800°C at 5–6 kbar in the Bunger Hills (Stüwe & Powell 1989). Slightly higher pressure conditions were proposed for the HJA (~700–750°C, 7–9 kbar) consistent with the observation of garnet within mafic granulite (Stüwe & Powell 1989, Sheraton *et al.* 1995). The timing of granulite facies metamorphism in the Bunger Hills is dated at 1190 ± 15 Ma from metamorphic zircon in one sample of tonalitic orthogneiss from Thomas Island (Sheraton *et al.* 1992) and is suggested to have accompanied D1 deformation (Stüwe & Powell 1989).

Despite the currently limited geochronological dataset from the Bunger Hills, many studies readily identify parallels between the timing of metamorphism and the emplacement age of Mesoproterozoic intrusive rocks in the Bunger Hills–HJA region with rocks in the

Table II. Bulk compositions used for phase equilibria modelling.

	Sample		
	6264	5607	6251
Whole rock geochemistry (wt%)*			
SiO_2	85.10	56.30	77.60
TiO_2	0.37	1.54	1.04
Al_2O_3	7.72	23.45	10.23
Fe_2O_3	0.25	3.49	1.30
FeO	1.33	7.79	3.29
MnO	0.02	0.11	0.06
MgO	1.05	3.09	1.84
CaO	0.41	2.07	0.81
Na_2O	0.63	1.00	1.02
K_2O	1.62	0.31	1.57
P_2O_5	0.01	0.05	0.01
LOI	0.84	0.76	0.81
Thermocalc input (mol%)			
H_2O	0.87	0.75	0.71
SiO_2	89.00	63.30	82.62
Al_2O_3	4.76	15.54	6.42
CaO	0.46	2.49	0.92
MgO	1.64	5.18	2.92
FeO	1.36	10.28	3.97
K_2O	1.08	0.22	1.07
Na_2O	0.64	1.09	1.05
TiO_2	0.29	1.30	0.83
O	0.10	0.15	0.52

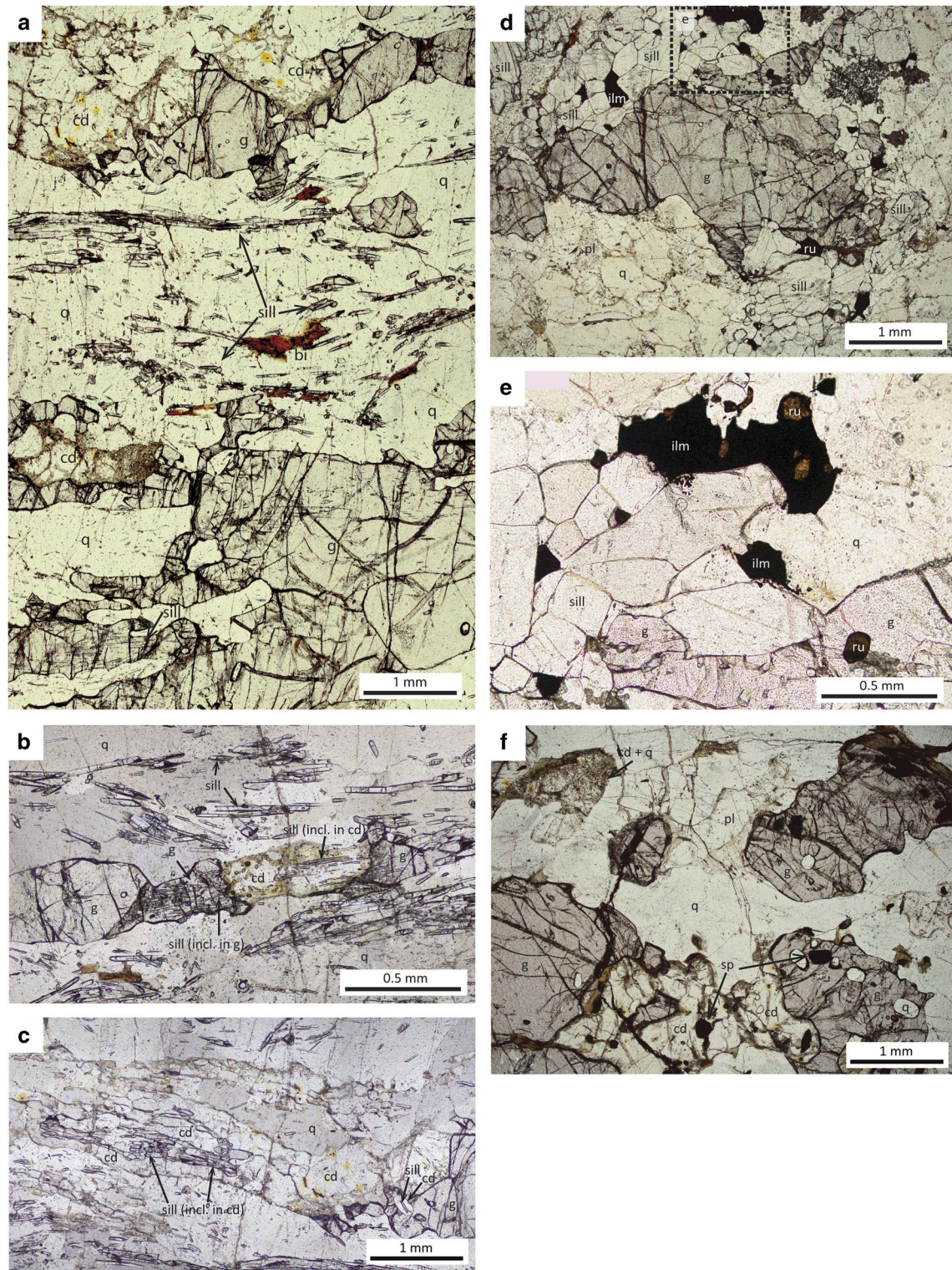*Reproduced from Sheraton *et al.* (1995)

Fig. 2. Representative thin section photomicrographs. **a.** Sample 6264: coarse, anhedral garnet grains are aligned with acicular sillimanite that defines the foliation. Cordierite grains (with included monazite showing yellow pleochroic halos) exhibit sharp grain boundaries and only occur adjacent to garnet. **b.** Sample 6264: anhedral cordierite bridging two garnet grains. Sillimanite is included within garnet and cordierite. **c.** Sample 6264: sillimanite completely hosted within cordierite. **d.** Sample 5607: coarse grained garnet is surrounded by idoblastic sillimanite, plagioclase and quartz. Ilmenite and rutile occur within the matrix and garnet grain edge. **e.** Sample 5607: anhedral ilmenite partially enclosing rutile. **f.** Sample 6251: cordierite occurs adjacent to coarse, anhedral garnet and in places completely surrounds smaller, relict garnet grains. Locally, cordierite occurs as symplectitic intergrowths with quartz. Minor spinel (< 200 μm) is included within both the garnet and cordierite. Mineral abbreviations from Holland & Powell (1998).

Windmill Islands in East Antarctica and Stage 2 of the Albany–Fraser Orogeny in south-west Australia (e.g. Sheraton *et al.* 1993, Clarke *et al.* 1995, Harris 1995, Clark *et al.* 2000, Fitzsimons 2000, 2003, Boger 2011). The Mesoproterozoic Albany–Fraser Orogeny is largely interpreted to record the final stages of assembly between the North and West Australian cratons with the combined South Australian Craton and East Antarctic Craton (Clark *et al.* 2000, Betts & Giles 2006, Cawood & Korsch 2008). Specifically, the Albany–Fraser Orogeny has been characterized by coeval felsic and mafic magmatism and high temperature, high pressure metamorphism pertaining to continental collision between 1345–1260 Ma (Stage 1) followed by intracratonic reactivation involving craton-vergent thrusting, high temperature metamorphism and predominantly felsic magmatism between 1215–1140 Ma (Stage 2; Nelson *et al.* 1995, Clark *et al.* 2000, Bodorkos & Clark 2004, Kirkland *et al.* 2011). More recently, however, the Albany–Fraser Orogeny has been suggested to have involved oceanic arc accretion onto the West Australian Craton (Spaggiari *et al.* 2015) and back-arc extensional tectonics (Clark *et al.* 2014, Spaggiari *et al.* 2015), rather than simply continental collision and intracratonic orogenesis. Stages 1 and 2 of the Albany–Fraser Orogeny in south-western Australia are also expressed as the Mount West Orogeny (*c.* 1345–1293 Ma) and Musgrave Orogeny (*c.* 1220–1150 Ma), respectively, in the Musgrave Inlier within central Australia (Smithies *et al.* 2011, Kirkland *et al.* 2013, Howard *et al.* 2015).

Sample descriptions

Samples utilized in this study comprise part of a suite of migmatized metasedimentary rocks collected during the 1986 Australian Antarctic research expedition to the Bunger Hills, Obruchev Hills and Denman Glacier region of East Antarctica and are archived at Geoscience Australia, Canberra. The three samples chosen for this study were collected from north of Raketa Island, Zabytyy Island and Geografov/Currituck Island in the HJA, directly north of the Bunger Hills (Fig. 1, Table I). These three samples are representative of the metapelitic lithologies that are interlayered with predominantly tonalitic orthogneiss within this region of the HJA. Whole rock geochemical analyses (reproduced from Sheraton *et al.* 1995; Table II) show a range from typical pelitic (sample 5607) to more felsic compositions (samples 6264 and 6251) that are more suggestive of impure sandstone–siltstone protoliths and/ or sampling of leucocratic-rich domains of a migmatite. Sample names are referred to by their last four digits throughout the text. Sample location grid references are provided in Table I. The mineralogy, age and peak metamorphic conditions of each sample are also summarized in Table I.

Sample 6264 (north Raketa Island)

Sample 6264 contains garnet, sillimanite, quartz, plagioclase, K-feldspar, ilmenite, and minor biotite and rutile. Garnet is coarse grained (up to 5 mm in length, ~ 5% abundance), typically elongate and contains partially to completely enclosed inclusions of sillimanite (Fig. 2a). Included sillimanite crystals are aligned with the external fabric as also defined by aggregates of sillimanite. Cordierite is often located adjacent to and separating garnet grains (e.g. Fig. 2a & b) and exhibits relatively sharp grain boundaries (Fig. 2a). Sometimes small grains of garnet are completely enclosed within the cordierite. Sillimanite is often also wholly included within cordierite occurring adjacent to garnet (e.g. Fig. 2c). Cordierite is never included within garnet. In places, fine grained (lamellae < 50 μm wide) cordierite–quartz symplectitic intergrowths also occur adjacent to garnet. The spatial relationship between garnet, cordierite and sillimanite is suggestive of the increased growth of cordierite following inferred peak growth of garnet and sillimanite. Rare, blocky rutile grains (~ 1 mm in length) occur in contact with sillimanite and are aligned with the fabric, but do not contain inclusions of sillimanite. Biotite is sparsely distributed and occurs as randomly oriented, anhedral grains (~ 200–1000 μm in length) along quartz–feldspar grain boundaries. The inferred peak mineral assemblage for this sample is garnet–sillimanite–ilmenite–rutile–plagioclase–K-feldspar–melt–quartz, with the post-peak development of cordierite after garnet and the inferred retrograde growth of biotite.

Sample 5607 (Geografov Island)

Sample 5607 contains sillimanite, garnet, rutile, ilmenite, quartz, plagioclase and rare biotite. Garnet is abundant (~ 25%) as very coarse grained (up to 1 cm in diameter), anhedral poikioblasts which host idioblastic sillimanite, coarse rutile (up to 500 μm), ilmenite and quartz (Fig. 2d). The modal abundance of rutile increases toward the garnet grain edge with many grains only occurring as partial inclusions within the garnet. In general, rutile occurring within garnet is coarser grained than rutile within the matrix (typically < 200 μm). Ilmenite is present throughout, but is typically more common external to garnet. Sometimes, ilmenite appears to form partial anhedral overgrowths about rutile (Fig. 2e). Sillimanite is ubiquitous and weakly aligned to define a coarse foliation. Rutile and ilmenite occur in direct contact with sillimanite, but are generally not included within individual sillimanite crystals. Biotite is rare, commonly occurring within fractures in garnet, and is accordingly inferred as being of retrograde origin. The peak metamorphic mineral assemblage for this sample is inferred to be garnet–sillimanite–ilmenite–rutile–plagioclase–melt–quartz.
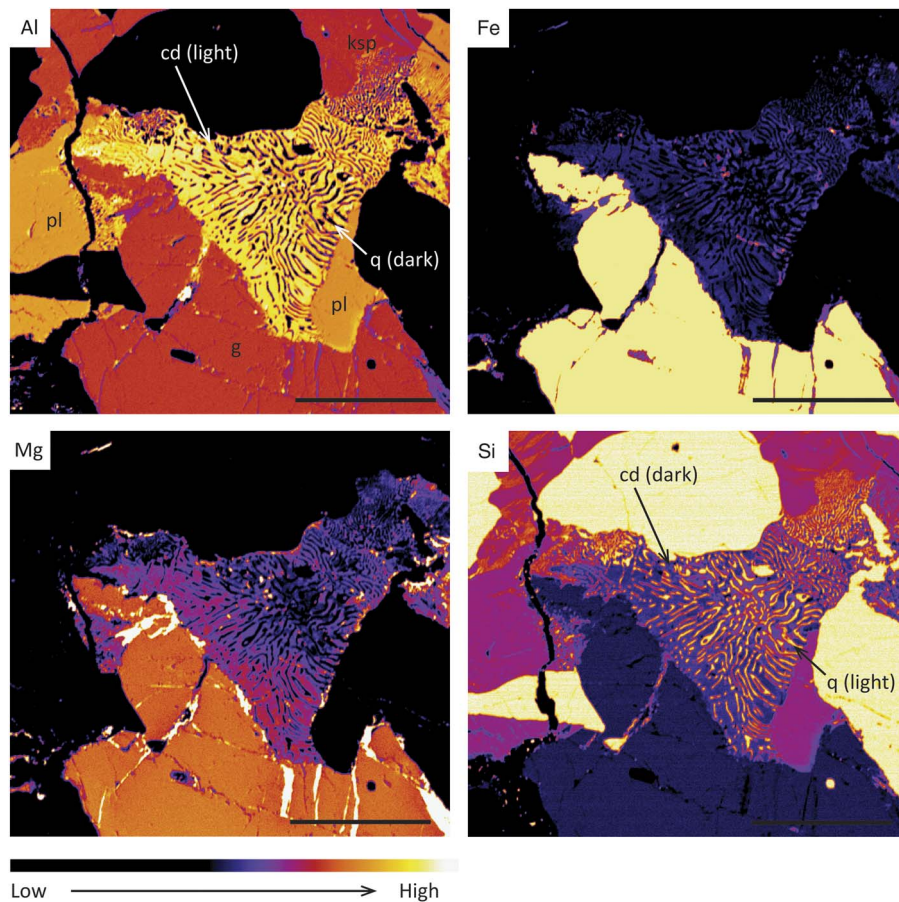
Fig. 3. Qualitative compositional maps of aluminium (Al), iron (Fe), magnesium (Mg) and silica (Si) which highlight the symplectitic intergrowth between cordierite and quartz adjacent to garnet in sample 6251. Dark colours represent low elemental abundance; warm colours represent high abundance. The black scale bar represents 1 mm. Mineral abbreviations from Holland & Powell (1998).

Sample 6251 (Zabytyy Island)

Sample 6251 contains garnet, spinel, cordierite, quartz, K-feldspar, plagioclase, and minor biotite, sillimanite and ilmenite. Garnet grains are moderately coarse grained (up to 2 mm diameter, ~5% abundance) and contain inclusions of minor amounts of dark green spinel (~100–200 µm in size, ~1% abundance) and rarely sillimanite (up to 250 µm length, <1% abundance). Spinel grains are also sometimes hosted within cordierite. Commonly, cordierite is anhedral and occurs adjacent to garnet with sharp grain boundaries (Fig. 2f) and/or sometimes as symplectitic intergrowths with quartz (e.g. Fig. 3). Garnet grains are also sometimes wholly included within cordierite (Fig. 2f). Similar to sample 6264, the observed microstructural relationships between garnet and cordierite are suggestive of the increased growth of cordierite after garnet and that some garnet grains are now potentially partially replaced by cordierite. Minor aggregates of subhedral cordierite grains also occur away from garnet and are aligned with the coarse foliation and considered to be preserved prograde–peak grains. Plagioclase is moderately abundant, occurring with quartz and minor K-feldspar as the main matrix phases. Biotite is subhedral (grains up to 1 mm in length) with no clear

preferred orientation. Grains are sparsely distributed and typically occur adjacent to ilmenite and at the grain boundaries of quartz and feldspar. The inferred peak mineral assemblage for this sample is garnet–cordierite–ilmenite–plagioclase–K-feldspar–melt–quartz. Post-peak mineral development is limited to the occurrence of randomly oriented biotite and the additional growth of cordierite after garnet. Spinel and sillimanite are interpreted to be potentially part of the prograde, but not peak, metamorphic mineral assemblage.

Analytical methods

Pressure–temperature conditions

Chemical compositions of minerals from all samples were obtained using a Cameca SX51 electron microprobe at Adelaide Microscopy, The University of Adelaide, using a beam current of 20 nA and an accelerating voltage of 15 kV. Elemental X-ray maps of sample 6251 were obtained using the same instrumentation, a 15 kV accelerating voltage and a beam current of 200 nA.

Calculations for P–T were completed using THERMOCALC version 3.37 with the internally

consistent updated thermodynamic dataset, ds62, of Holland & Powell (2011), for the geologically realistic system of NCKFMASHTO (Na_2O–CaO–K_2O–FeO–MgO–Al_2O_3–SiO_2–H_2O–TiO_2–Fe_2O_3), and using the activity relationships of White *et al.* (2014). The bulk compositions used for P–T pseudosection calculations are based on the whole rock XRF geochemical analyses (Table II) of each sample from Sheraton *et al.* (1995) recalculated to molar oxide percent.

A variety of published methods in metamorphic phase diagram literature are employed to estimate the H_2O content in bulk compositions used in phase equilibria modelling (e.g. Kelsey & Hand 2015 and references therein). In this study, the H_2O content for each sample was approximated from the abundance and chemical compositions of hydrous minerals in the observed mineral assemblages. The sensitivity of the chosen H_2O content on the phase equilibria, namely the influence of H_2O on the temperature of the solidus, and the range of H_2O contents required to develop the observed peak mineral assemblage, is also evaluated for each sample using a calculated Temperature–M_{H2O} diagram (Fig. S1 found at http://dx.doi.org/10.1017/S095410201600033X). The Fe_2O_3 content for each sample was selected by an approximation of the abundance and stoichiometrically recast (Droop 1987) electron microprobe compositions of Fe^{3+}-bearing minerals in each sample. A Temperature–XFe_2O_3 (XFe_2O_3 = Fe_2O_3/(FeO + Fe_2O_3)) diagram is also presented for each sample in Fig. S2 (found at http://dx.doi.org/10.1017/S095410201600033X). This allows for assessment of the change in stability of the preserved mineral assemblages with variation of the Fe oxidation state from all Fe existing as FeO to all Fe as Fe_2O_3, and a comparison with the selected Fe_2O_3 content estimated from mineral compositions and abundance. The bulk compositions used for P–T pseudosection calculations are provided in Table II. Compositional isopleths and modal proportions of minerals were calculated using software TCInvestigator (version 1; Pearce *et al.* 2015; Fig. S3 found at http://dx.doi.org/10.1017/S095410201600033X) to further constrain the P–T conditions.

Laser ablation inductively coupled plasma mass spectrometry monazite geochronology

Monazite grains were imaged using a back-scattered electron (BSE) detector on a Phillips XL30 SEM. *In situ* monazite geochronology was undertaken using laser ablation inductively coupled plasma mass spectrometry (LA–ICP–MS) at Adelaide Microscopy, The University of Adelaide, following the methods of Payne *et al.* (2008). U-Pb analyses were acquired using a New Wave 213 nm Nd–YAG laser coupled with an Agilent 7500cs ICP–MS under a He-ablation atmosphere. Analyses involved 40 s of background measurement, including 10 s of the laser

firing with the shutter closed to allow for beam stabilization, followed by 40 s of ablation. Ablation was performed with a frequency of 5 Hz and a spot size of 12 μm. Isotopes ^{204}Pb, ^{206}Pb, ^{207}Pb and ^{238}U were measured for 10 ms, 15 ms, 30 ms and 15 ms, respectively.

The primary monazite standard MAdel (TIMS normalization data: $^{207}Pb/^{206}Pa$ = 490.0 Ma, $^{206}Pb/^{238}U$ = 518.4 Ma and $^{207}Pb/^{235}U$ = 513.1 Ma; Payne *et al.* 2008, updated with additional TIMS data) was used to correct for elemental fractionation and mass bias of the monazite data using software 'Glitter' (Griffin *et al.* 2008). Accuracy was monitored by repeat analysis of the in-house standard 94-222/Bruna NW (*c.* 450 Ma, Payne *et al.* 2008). Over the duration of the study, the MAdel analyses yielded a weighted mean age of $^{207}Pb/^{206}Pb$ = 490.5 ± 9.2 Ma, $^{206}Pb/^{238}U$ = 517.2 ± 3.2 Ma and $^{207}Pb/^{235}U$ = 512.3 ± 2.6 Ma (n = 32), and secondary standard 94-222/Bruna NW yielded weighted

Table III. Summary of mineral chemistry.

	Sample		
	6264	5607	6251
Garnet core			
X_{alm}	0.54–0.57	0.60–0.65	0.55–0.57
X_{py}	0.40–0.42	0.3–0.35	0.36–0.39
X_{gr}	0.03–0.033	0.039–0.047	0.025–0.038
X_{spss}	0.01–0.015	0.08–0.1	0.02
Garnet rim			
X_{alm}	0.54–0.55	0.60–0.63	0.57–0.63
X_{py}	0.39–0.42	0.3–0.35	0.31–0.37
X_{gr}	0.029–0.033	0.04–0.062	0.029–0.033
X_{spss}	0.01–0.015	0.08–0.1	0.02
Biotite			
X_{Fe}	0.21–0.25	0.22–0.24	0.27–0.38
Al_2O_3 (wt%)	13.41–15.03	15.46–16.01	15.82–16.80
MnO (wt%)	0–0.03	0–0.01	0–0.01
TiO_2 (wt%)	3.12–4.65	4.13–4.76	3.69–4.85
F (wt%)	2.37–2.76	0.57–0.53	0.56–0.96
K-feldspar			
X_{an}	0.0–0.01	-	0–0.01
X_{or}	0.80–0.91	-	0.88–0.92
Plagioclase			
X_{an}	0.38–0.40	0.41–0.50	0.27–0.33
X_{or}	0.01	0.01–0.03	0.01–0.06
Ilmenite			
MnO (wt%)	0	0.06–0.1	0.03–0.65
Cordierite			
X_{Fe}	0.16–0.2	-	0.15–0.18
Spinel			
ZnO (wt%)	-	-	0.97–1.17
X_{gah}	-	-	0.02
X_{sp}	-	-	0.31–0.43
Cr_2O_3 (wt%)	-	-	0.19–1.04
MnO (wt%)	-	-	0.01–0.1

Abbreviations: X_{alm} = Fe^{2+}/(Fe^{2+} + Mg + Ca + Mn), X_{py} = Mg/(Fe^{2+} + Mg + Ca + Mn), X_{gr} = Ca/(Fe^{2+} + Mg + Ca + Mn), X_{spss} = Mn/(Fe^{2+} + Mg + Ca + Mn), X_{Fe} = Fe^{2+}/(Fe^{2+} + Mg), X_{An} = Ca/(Ca + Na + K), X_{Or} = K/(Ca + Na + K), X_{gah} = Zn/(Zn + Mg + Al + Ti), X_{sp} = Mg/(Fe^{2+} + Mg).
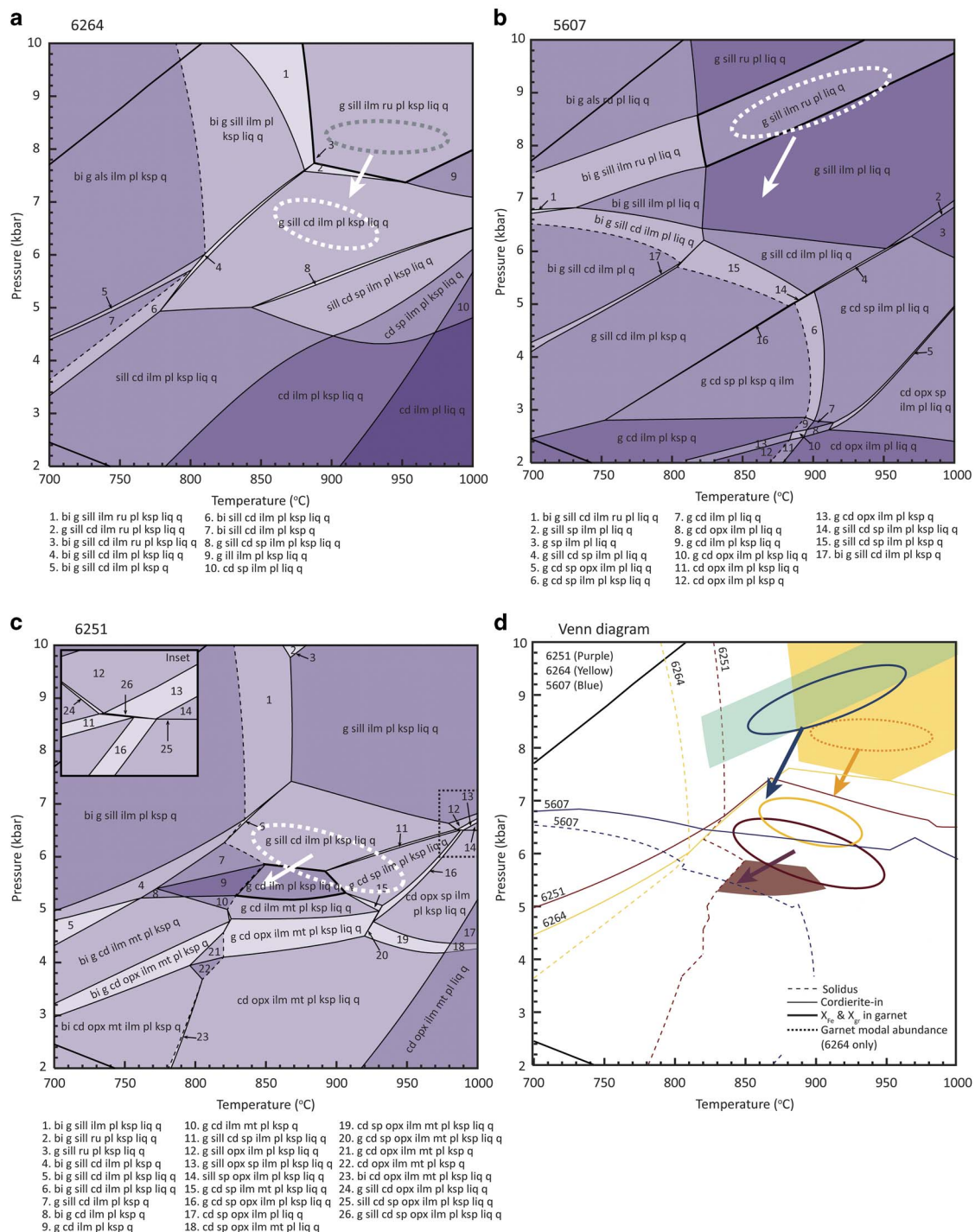
Fig. 4. Pressure–temperature (P–T) pseudosections constructed for **a.** sample 6264, **b.** sample 5607 and **c.** sample 6251. Bulk compositions used for the calculation of each pseudosection are provided in Table II. The solidus is shown as a black dashed line. The stability field of the inferred peak mineral assemblage in each sample is outlined in bold. The approximate range of peak P–T conditions on the basis of X_{Fe} and X_{gr} compositional isopleths in garnet and garnet modal abundance is indicated by dashed white circles in b. and c. In a., the peak P–T conditions constrained from garnet compositional isopleths are shown as a white dashed circle; P–T conditions corresponding to observed garnet modal proportions are represented by the grey dashed circle. White arrows reflect the inferred P–T path constrained from microstructural mineral relationships. **d.** Summary of P–T conditions from all samples. The inferred peak mineral assemblage stability fields corresponding to each sample (shaded regions), P–T constraints from garnet compositional isopleths (solid open circles) and modal proportions where different (open dashed circle for sample 6264) are superimposed. Inferred P–T paths for each sample are shown. Cordierite-in lines from a.–c. are also shown as cordierite is used as a constraint on the P–T path. Sample 6264 is represented in yellow, sample 5607 in blue and sample 6251 in purple. Mineral abbreviations are from Holland & Powell (1998).

mean ages of $^{207}Pb/^{206}Pb = 451 \pm 15$ Ma, $^{206}Pb/^{238}U = 460 \pm 12$ Ma and $^{207}Pb/^{235}U = 459 \pm 12$ Ma ($n = 12$). Instrument drift was corrected for by bracketing every ten unknowns with standard analyses and applying a linear correction. Due to unresolvable interference of ^{204}Hg on ^{204}Pb, a common Pb correction was not applied; however, ^{204}Pb was monitored to assess the common lead of each analysis and analyses were rejected if anomalous ^{204}Pb was observed relative to background levels.

Results

Mineral chemistry

A summary of mineral compositions from all samples is provided in Table III. Full representative analyses for each mineral are presented in Table S1 (found at http://dx. doi.org/10.1017/S095410201600033X). The chemistry of select minerals is discussed as follows.

Garnet grains from sample 6251 show slight core–rim enrichment in X_{alm} ($Fe^{2+}/(Fe^{2+} + Ca + Mg + Mn)$), and generally, depletion in X_{py} ($Mg/(Fe^{2+} + Ca + Mg + Mn)$) and X_{gr} ($Ca/(Fe^{2+} + Ca + Mg + Mn)$) with values of 0.55–0.57, 0.36–0.39 and 0.025–0.038 obtained from garnet cores and values of 0.57–0.63, 0.31–0.37 and 0.029–0.033 from garnet rims, respectively. Garnet from samples 6264 and 5607 do not exhibit any appreciable core–rim compositional zoning. In sample 6264, X_{alm} ranges between 0.54–0.57, X_{py} between 0.39–0.42, X_{gr} between 0.029–0.033 and X_{spss} ($Mn/(Fe^{2+} + Ca + Mg + Mn)$) between 0.01–0.015. In sample 5607, X_{alm} ranges between 0.60–0.65, X_{py} between 0.30–0.35, X_{gr} between 0.039–0.062 and X_{spss} between 0.08–0.1.

Biotite in all samples is magnesian with X_{Fe} ($Fe^{2+}/(Fe^{2+} + Mg)$) values ranging between 0.21–0.25 in sample 6264, 0.22–0.24 in sample 5607 and 0.27–0.38 in sample 6251. Throughout all samples, TiO_2 values are moderately high and range between 3.12–4.85 wt%. Biotite in samples 5607 and 6251 exhibit relatively low F contents, between 0.53–0.57 wt% and 0.56–0.96 wt%, respectively; F values range between 2.37–2.76 wt% in sample 6264.

K-feldspar is found in samples 6264 and 6251. K-feldspar is K-rich and Ca-poor with X_{an} ($Ca/(Ca + Na + K)$) of 0–0.01 and X_{or} ($K/(Ca + Na + K)$) of 0.80–0.92 in both samples. Plagioclase is present in all three samples and is Na-rich with X_{an} values between 0.38–0.40, 0.41–0.51 and 0.27–0.33 in samples 6264, 5607 and 6251, respectively. X_{or} values in plagioclase range from 0.01–0.06.

Cordierite occurs in samples 6264 and 6251. Cordierite is magnesian in composition with X_{Fe} values between 0.15–0.20 and no apparent variation in composition between cores or rims.

Ilmenite has a low MnO content in all samples, ranging from 0–0.65 wt%.

Spinel occurs in sample 6251. Spinel contains a moderate amount of ZnO, ranging from 0.97–1.17 wt% and with a X_{gah} ($Zn/(Zn + Fe^{2+} + Mg + Mn)$) value of 0.02. X_{sp} ($Mg/(Zn + Fe^{2+} + Mg + Mn)$) ranges from 0.31–0.43 wt%, Cr_2O_3 varies between 0.19–1.04 wt% and MnO varies between 0.01–0.1 wt%.

Pressure–temperature conditions

$T–XFe_2O_3$ diagrams used for the determination of ferric iron in the bulk composition of each sample are shown in Fig. S2. Calculated P–T pseudosections for each sample are presented in Fig. 4a–c and are contoured for X_{gr} and X_{Fe} in garnet and modal proportions of relevant phases in Fig. S3. Superimposed pseudosection peak mineral assemblage stability fields for all samples are shown in Fig. 4d for comparison.

In sample 6264 (Fig. 4a), the garnet stability field is broad, extending to pressures above ~ 5 kbar over the range 700–1000°C. Decreasing garnet abundance with decreasing pressure is associated with an increase in X_{Fe} in garnet and consistently low X_{gr} (Fig. S3). Cordierite is present at pressures lower than ~ 4.5 kbar at 700°C and the range of stable pressures increases with temperature. The occurrence of rutile is restricted to pressures higher than ~ 7 kbar and temperatures > 850°C. The interpreted peak metamorphic assemblage garnet–sillimanite–ilmenite–rutile–plagioclase–K-feldspar–melt–quartz for this sample is stable at > 900°C and > 7 kbar. These P–T conditions are in agreement with calculated garnet modal proportions and petrographic observations, which suggest $\sim 5\%$ garnet abundance in this sample. However, chemical compositions of X_{Fe} and X_{gr} from unzoned garnet cores suggest P–T conditions of ~ 850–950°C at ~ 6–7 kbar, occurring within the lower pressure field garnet–sillimanite–cordierite–ilmenite–plagioclase–K-feldspar–melt–quartz. This P–T estimate is inconsistent with the presence of rutile and the inferred absence of peak cordierite in this sample. Cordierite is inferred to have grown during post-peak metamorphism at the expense of garnet ± sillimanite (e.g. Fig. 2a & b). This relationship corresponds to a simultaneous increase in the modal proportion of cordierite and a decrease in garnet and sillimanite; thus it suggests that this rock evolved through a broadly decompressional retrograde P–T path (Figs 4a & S3).

In sample 5607 (Fig. 4b), rutile-bearing assemblages occur at pressures > 7 kbar at 700°C with rutile stability contracting to higher pressures with increasing temperature. Ilmenite is present below 7.5 kbar at 700°C and occurs at higher pressures with increasing temperature, coexisting with rutile only over a narrow pressure range (~ 1 kbar). Garnet is present throughout the majority of the pseudosection. The inferred peak mineral assemblage garnet–sillimanite–ilmenite–rutile–plagioclase–melt–quartz for this sample exists over a narrow P–T range extending

from ~7.5–8.5 kbar at 850°C, to >9.5 kbar at 1000°C. Modal proportions of garnet and X_{gr} and X_{Fe} compositions from unzoned garnet cores are in agreement with this P–T estimate. In this sample, a lower abundance of rutile is observed within the matrix relative to rutile included within garnet, and anhedral ilmenite overgrowths occur on some rutile grains (e.g. Fig. 2e). This reflects a decreasing modal proportion of rutile and an increase in the abundance of ilmenite following growth of peak metamorphic garnet.

Comparison with calculated mineral modal proportions therefore also suggests a decompressional post-peak evolution for this rock.

In sample 6251 (Fig. 4c), garnet exists at pressures >3 kbar at 700°C and contracts to higher pressures with increasing temperature. Cordierite stability occurs below 7 kbar while sillimanite is restricted to pressures greater than ~5.5–6.5 kbar. Spinel is present at ~900°C at 5.5 kbar, with the range of stable pressures widening to

Table IV. Laser ablation inductively coupled plasma mass spectrometry U-Pb *in situ* monazite geochronology.

Analysis	Location	$^{207}Pb/^{206}Pb$	1σ	$^{206}Pb/^{238}U$	1σ	$^{207}Pb/^{235}U$	1σ	^{204}Pb (cps)	Age (Ma)						Conc. (%)
									$^{207}Pb/^{206}Pb$	1σ	$^{206}Pb/^{238}U$	1σ	$^{207}Pb/^{235}U$	1σ	
6251.1.1	g	0.07919	0.00084	0.20115	0.00278	2.19633	0.03051	0	1177	21	1182	15	1180	10	100
6251.1.2	g	0.07892	0.00090	0.20436	0.00285	2.22363	0.03228	5	1170	23	1199	15	1189	10	102
6251.2.1	g	0.07901	0.00084	0.19607	0.00271	2.13577	0.02988	0	1172	21	1154	15	1161	10	98
6251.2.2	g	0.07970	0.00085	0.19442	0.00269	2.13627	0.02990	0	1190	21	1145	15	1161	10	96
6251.2.3	g	0.07924	0.00086	0.19653	0.00272	2.14713	0.03026	0	1178	21	1157	15	1164	10	98
6251.2.4	g	0.07897	0.00086	0.19829	0.00275	2.15897	0.03051	0	1172	21	1166	15	1168	10	100
6251.3.1	m	0.08046	0.00088	0.19387	0.00269	2.15055	0.03047	7	1208	21	1142	15	1165	10	95
6251.3.2	m	0.08009	0.00095	0.19834	0.00278	2.18992	0.03243	1	1199	23	1166	15	1178	10	97
6251.5.1	m	0.08969	0.00122	0.20053	0.00287	2.47959	0.03998	10	1419	26	1178	15	1266	12	83
6251.6.1	g	0.08029	0.00091	0.20864	0.00291	2.30940	0.03345	5	1204	22	1222	16	1215	10	101
6251.6.2	g	0.08331	0.00098	0.21613	0.00303	2.48240	0.03682	11	1276	23	1261	16	1267	11	99
6251.7.1	g	0.08035	0.00096	0.21280	0.00298	2.35717	0.03525	13	1206	23	1244	16	1230	11	103
6251.7.2	g	0.07988	0.00097	0.21338	0.00300	2.34986	0.03540	2	1194	24	1247	16	1228	11	104
6251.7.3	g	0.08178	0.00102	0.20288	0.00286	2.28725	0.03510	13	1240	24	1191	15	1208	11	96
6251.8.1	g	0.07966	0.00086	0.21652	0.00288	2.37691	0.03223	7	1189	21	1264	15	1236	10	106
6251.8.2	g	0.07834	0.00084	0.19398	0.00257	2.09443	0.02822	3	1156	21	1143	14	1147	9	99
6251.11.1	g	0.07969	0.00090	0.19972	0.00264	2.19349	0.03016	0	1189	22	1174	14	1179	10	99
6251.11.2	g	0.07849	0.00088	0.19954	0.00263	2.15856	0.02960	0	1159	22	1173	14	1168	10	101
6264.1.1	m	0.07822	0.00086	0.20333	0.00266	2.19225	0.02950	18	1153	22	1193	14	1179	9	104
6264.2.2	m	0.07818	0.00089	0.18190	0.00237	1.96006	0.02680	5	1152	23	1077	13	1102	9	94
6264.3.1	g	0.07639	0.00085	0.17461	0.00225	1.83852	0.02461	9	1105	22	1037	12	1059	9	94
6264.4.1	g	0.07935	0.00089	0.19984	0.00257	2.18558	0.02925	8	1181	22	1175	14	1177	9	99
6264.5.1	m	0.07949	0.00092	0.20882	0.00268	2.28792	0.03105	0	1184	23	1223	14	1209	10	103
6264.7.1	m	0.07912	0.00085	0.20329	0.00272	2.21682	0.03007	9	1175	21	1193	15	1186	9	102
6264.7.2	m	0.07840	0.00085	0.18958	0.00253	2.04835	0.02785	4	1157	21	1119	14	1132	9	97
6264.8.1	m	0.08079	0.00093	0.20170	0.00270	2.24574	0.03156	9	1216	22	1184	14	1196	10	97
6264.8.2	m	0.07863	0.00102	0.21992	0.00298	2.38332	0.03608	0	1163	26	1281	16	1238	11	110
6264.8.3	m	0.07981	0.00096	0.20117	0.00269	2.21289	0.03170	4	1192	23	1182	14	1185	10	99
6264.9.1	m	0.08038	0.00090	0.19802	0.00262	2.19378	0.03014	0	1206	22	1165	14	1179	10	97
6264.9.2	m	0.07917	0.00090	0.18916	0.00249	2.06412	0.02841	2	1177	22	1117	14	1137	9	95
6264.10.1	m	0.07928	0.00089	0.20945	0.00275	2.28850	0.03122	13	1179	22	1226	15	1209	10	104
6264.12.1	m	0.08092	0.00089	0.20606	0.00269	2.29810	0.03097	2	1220	22	1208	14	1212	10	99
6264.12.2	m	0.08034	0.00090	0.19054	0.00248	2.10978	0.02852	7	1205	22	1124	13	1152	9	93
6264.11.1	m	0.08098	0.00091	0.19876	0.00258	2.21826	0.03006	44	1221	22	1169	14	1187	9	96
6264.11.2	m	0.08007	0.00091	0.18722	0.00243	2.06615	0.02812	8	1199	22	1106	13	1138	9	92
5607.1.1	g	0.07962	0.00109	0.21197	0.00291	2.32576	0.03646	3	1188	27	1239	15	1220	11	104
5607.1.2	g	0.07792	0.00107	0.20024	0.00274	2.15002	0.03382	1	1145	27	1177	15	1165	11	103
5607.2.1	g	0.07938	0.00098	0.19457	0.00262	2.12833	0.03105	0	1182	24	1146	14	1158	10	97
5607.2.2	g	0.07856	0.00095	0.19466	0.00261	2.10732	0.03044	3	1161	24	1147	14	1151	10	99
5607.3.1	m	0.07896	0.00105	0.19384	0.00263	2.10924	0.03238	0	1171	26	1142	14	1152	11	98
5607.3.2	m	0.07928	0.00115	0.18763	0.00258	2.04997	0.03323	18	1179	28	1109	14	1132	11	94
5607.3.3	m	0.07843	0.00088	0.18895	0.00250	2.04215	0.02814	0	1158	22	1116	14	1130	9	96
5607.3.4	m	0.07880	0.00093	0.18105	0.00241	1.96594	0.02780	0	1167	23	1073	13	1104	10	92
5607.5.1	g	0.07864	0.00135	0.17885	0.00253	1.93823	0.03555	0	1163	34	1061	14	1094	12	91
5607.6.1	g	0.07565	0.00094	0.19374	0.00259	2.01977	0.02954	0	1086	25	1142	14	1122	10	105
5607.6.2	g	0.07715	0.00096	0.19129	0.00255	2.03360	0.02970	4	1125	25	1128	14	1127	10	100
5607.7.1	g	0.10188	0.00163	0.20907	0.00295	2.93501	0.05072	30	1659	29	1224	16	1391	13	74

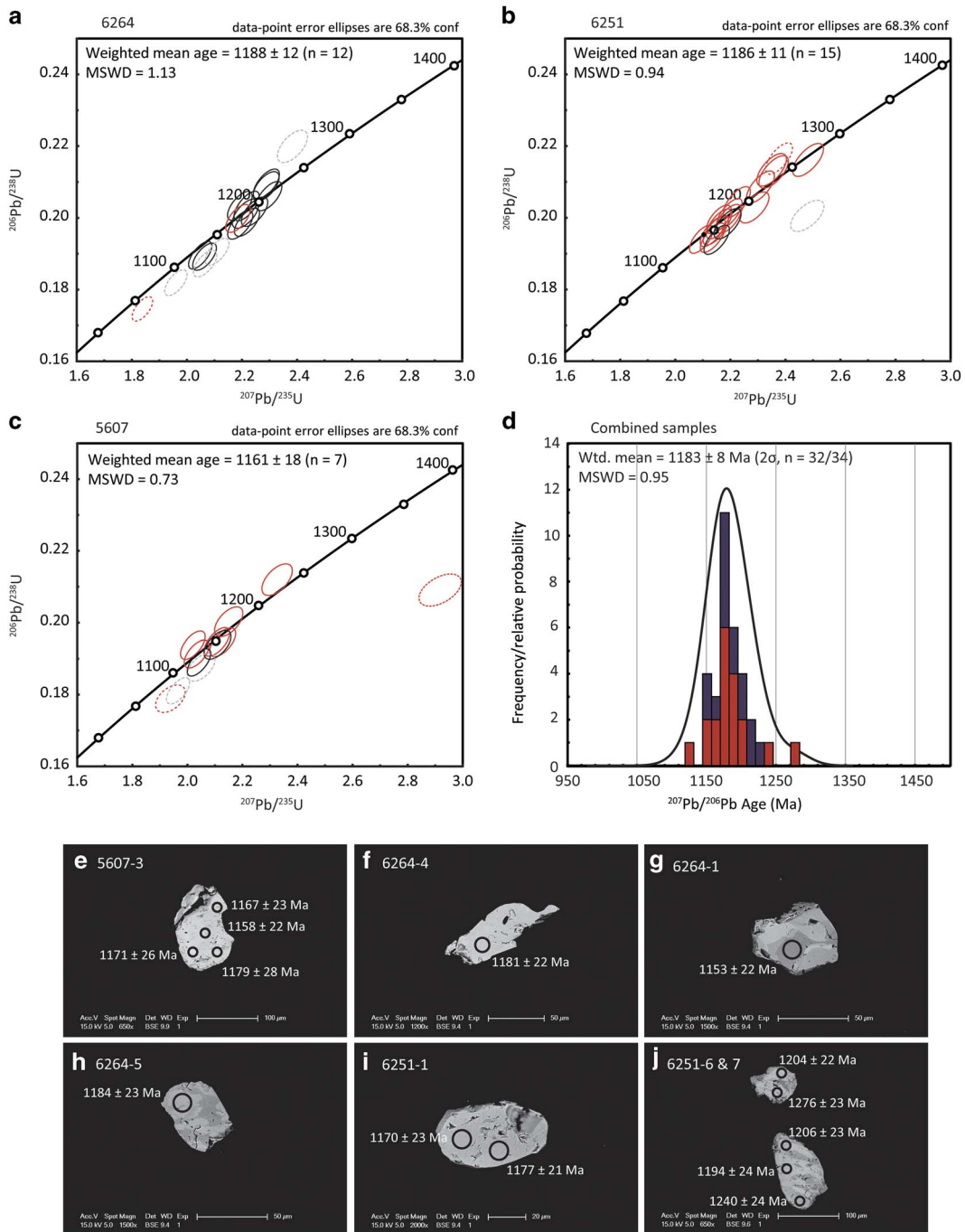Abbreviations: g = monazite hosted within garnet, m = matrix monazite

Fig. 5. *In situ* LA-ICP-MS monazite U-Pb geochronology. Data are presented on U-Pb concordia diagrams: **a.** sample 6264, **b.** sample 6251 and **c.** sample 5607. Red ellipses represent analyses from monazite included within garnet; black ellipses represent analyses from matrix monazite. Red and grey ellipses shown with a dashed outline represent analyses that are >5% discordant from monazite hosted in garnet and matrix monazite, respectively. Weighted mean ^{207}Pb/^{206}Pb ages are given for the combined concordant analyses from each sample. **d.** Histogram and probability density distribution plot for monazite age data from all three samples. Analyses from monazite grains included within garnet are shown in red; analyses from monazite included within matrix minerals are shown in blue. Collectively, the age data define a single population which yields a weighted mean ^{207}Pb/^{206}Pb age of 1183 ± 8 Ma. **e.–j.** Representative BSE images of analysed monazite grains from all samples. Open black circles represent the approximate location of U-Pb analyses. Corresponding ^{207}Pb/^{206}Pb U-Pb ages are shown. Age uncertainties are given at the 1σ level.

between ~ 4–7 kbar at 1000°C. The inferred peak mineral assemblage garnet–cordierite–ilmenite–plagioclase–K-feldspar–melt–quartz exists over a small P–T range between ~ 830–900°C and 5.2–5.8 kbar. However, chemical compositions of X_{Fe} and X_{gr} from garnet suggest that peak conditions were ~ 850–950°C and 5.4–6.6 kbar, occurring at a slightly higher pressure than the inferred peak assemblage field, within the garnet–sillimanite–cordierite–ilmenite–plagioclase–K-feldspar–melt–quartz-bearing field or adjacent spinel-bearing, sillimanite–absent field. Calculated modal proportions and estimated abundance of garnet and peak cordierite in this sample are in agreement with the peak conditions estimated from the garnet compositional isopleths. Similar to sample 6264, the inferred growth of cordierite after garnet (e.g. Figs 2f & 3) is suggestive of a broadly decompressional retrograde P–T path for this sample. The absence of magnetite in this sample constrains this down-temperature P–T path to have tracked along a relatively shallow P–T trajectory, above ~ 5 kbar.

Monazite U-Pb LA–ICP–MS geochronology

In situ monazite LA–ICP–MS was undertaken on samples 6251, 6264 and 5607 (Table IV, Fig. 5a–d). Monazite is sparse in all samples, and when present, typically occurs within and along the grain boundaries of matrix minerals. Rarely, monazite is partially hosted within garnet. Representative BSE images of analysed monazites are given in Fig. 5e–j. A few grains exhibit indistinct internal core–rim style zonation; however, the majority of grains appear unzoned in BSE imagery. The monazite grains do not show any relationship between their microstructural location and age. Weighted average calculations use the $^{207}Pb/^{206}Pb$ age. Concordia diagrams for each sample and a probability density plot of the combined age data are presented in Fig. 5a–d. Collectively, analyses that are ≤ 5% discordant yield a weighted mean age of 1183 ± 8 Ma ($n = 32/34$, mean square weighted deviation (MSWD) = 0.95).

In sample 6264, 15 analyses were done on nine grains within the matrix and two analyses from two grains hosted within garnet. Grains are ~ 40–100 μm in size and sub-rounded to elongate in shape. Some grains display subtle, patchy internal zonation visible in BSE imagery. Five analyses that are > 5% discordant are excluded from weighted mean calculations. The remaining 12 analyses range between 1221 ± 22 Ma and 1153 ± 22 Ma and give a $^{207}Pb/^{206}Pb$ weighted average age of 1188 ± 12 Ma (MSWD = 1.13; Fig. 5a).

In sample 6251, 15 analyses were obtained from five grains located partially and completely within garnet and three analyses from three grains within the foliated matrix. Grains are commonly ~ 30–100 μm in diameter, sub-rounded, generally unzoned in BSE imagery and are commonly pitted or cracked. Two analyses that are

> 5% discordant (analysis 6251.5.1 and 6251.8.1) and one outlying, older concordant analysis (analysis 6251.6.1, 1276 ± 23 Ma) are excluded from weighted mean calculations. The remaining analyses range between 1240 ± 24 Ma and 1156 ± 21 Ma ($n = 15$) and yield a $^{207}Pb/^{206}Pb$ weighted mean age of 1186 ± 11 Ma (MSWD = 0.94; Fig. 5b).

In sample 5607, eight analyses were collected from five grains hosted within garnet and four analyses from one grain within the matrix. Grains are ~ 40–60 μm in size, largely unzoned in BSE imagery, anhedral in shape and are commonly pitted and fractured. Four analyses that are > 5% discordant (analysis 5607.3.2, 3.4, 5.1 and 7.1) and one anomalously young, concordant analysis (analysis 5607.6.1, 1086 ± 25 Ma) are excluded from weighted mean age calculations. The remaining seven analyses range between 1188 ± 27 Ma and 1125 ± 25 Ma and give a $^{207}Pb/^{206}Pb$ weighted average age of 1161 ± 18 Ma (MSWD = 0.73; Fig. 5c).

Discussion

Age of metamorphism

In situ U-Pb monazite ages obtained in this study range predominantly between *c.* 1240–1150 Ma and give a weighted average $^{207}Pb/^{206}Pb$ age of 1183 ± 8 Ma. This mean age is within error of the age of metamorphism previously determined for the Bunger Hills from metamorphic zircon in tonalitic orthogneiss (Sheraton *et al.* 1992). The timing of metamorphism within this study is also similar to the age of Mesoproterozoic metamorphism and magmatism recorded elsewhere within the MAFO (e.g. Clark *et al.* 2000, Kirkland *et al.* 2011, 2013, Smithies *et al.* 2011, Tucker *et al.* 2015, Walsh *et al.* 2015). Previous studies have utilized SHRIMP zircon, monazite and rutile geochronology to ascertain that, specifically, the Mesoproterozoic Albany–Fraser Orogeny in south-western Australia was characterized by two discrete thermotectonic pulses at *c.* 1345–1260 Ma (Stage 1) and *c.* 1214–1140 Ma (Stage 2; Nelson *et al.* 1995, Clark *et al.* 2000, Kirkland *et al.* 2011). Tectonism of a similar age is recorded by felsic gneiss and charnokite (*c.* 1380–1180 Ma) from the Windmill Islands in East Antarctica (Post 2000, Zhang *et al.* 2012). Evidence for widespread felsic magmatism at *c.* 1345–1293 Ma (Mount West Orogeny) and *c.* 1220–1150 Ma (Musgrave Orogeny) also occurs within the Musgrave Inlier (Smithies *et al.* 2011, Kirkland *et al.* 2013, Howard *et al.* 2015), with the latter also linked with pervasive high temperature to ultra-high temperature metamorphism (Tucker *et al.* 2015, Walsh *et al.* 2015).

The Bunger Hills, HJA and Windmill Islands in East Antarctica have been correlated along strike of the Nornalup Complex of the MAFO in Gondwanan

tectonic reconstructions (e.g. Clarke *et al.* 1995, Harris 1995, Fitzsimons 2003). Stage 1 tectonism in the Nornalup Complex is recorded by the Malcolm Gneiss (Clark *et al.* 2000) and the earliest evidence for Recherche Supersuite magmatism (1330 ± 14 Ma; Nelson *et al.* 1995). The Nornalup Complex is otherwise dominated by Stage 2 tectonism as evidenced by the emplacement of the Esperance Supersuite, amphibolite facies metamorphism of sedimentary rocks from Mount Ragged (1154 ± 15 Ma; Clark *et al.* 2000) and granulite facies metamorphism of the garnet–cordierite-bearing Salisbury Gneiss (*c.* 1215 Ma and *c.* 1180 Ma; Clark *et al.* 2000). Geometric considerations suggest that the Stage 1 tectonothermal events recognized in the Windmill Islands and Nornalup Complex, therefore, possibly also affected the Bunger Hills and HJA. However, the results from this study and those obtained previously by Sheraton *et al.* (1992) suggest that the Bunger Hills records only the second stage of the Albany–Fraser Orogeny, with magmatism and metamorphism occurring between *c.* 1190–1150 Ma. More geochronological data is required to determine conclusively whether the apparent absence of *c.* 1300 Ma tectonism in the Bunger Hills–HJA region is geologically important or if it is merely a reflection of a current paucity in age data.

New metamorphic constraints for the HighJump Archipelago

The rocks of the HJA experienced intermediate pressure, granulite facies metamorphism (~ 850–950°C, 6–9 kbar; Fig. 4d). The highest pressure conditions are recorded by a sample of garnet–sillimanite–rutile-bearing gneiss (sample 5607) from Geografov Island (~ 850–950°C, 8–10 kbar). The metamorphic conditions recorded by samples 6264 and 6251 from north of Raketa Island and Zabytyy Island, respectively, are inferred to have occurred at a slightly lower pressure relative to sample 5607 (Fig. 4d). However, the exact peak metamorphic conditions of these two samples are less assuredly constrained due to some inconsistencies between the calculated P–T pseudosections, measured garnet compositions and petrographic observations. The inferred peak mineral assemblage in sample 6264 is stable at P–T conditions > 900°C and > 7 kbar, with estimated garnet abundance ($\sim 5\%$ abundance) further constraining P–T conditions to the lower pressure region of this field (~ 7–8 kbar). Considering that some garnet grains are potentially now partially replaced by cordierite, this P–T estimate is in effect a minimum with peak P–T conditions probably occurring at an even higher pressure. Therefore, on the basis of garnet modal proportions, the lower pressure boundary of the inferred peak mineral assemblage field defines the minimum limit on the peak metamorphic conditions. In contrast, measured X_{Fe} and X_{gr} garnet chemical compositions

from sample 6264 suggest that peak metamorphic conditions were 850–950°C and 6–7 kbar, within the adjacent cordierite-present field. Given the relatively small size of garnet grains in this sample (typically 1–5 mm) and the ability of garnet to be compositionally reset under even short-lived granulite facies metamorphism (e.g. Spear 1991, Caddick *et al.* 2010), it is probable that these garnets now record a modified composition resulting from diffusion during cooling from slightly higher pressure, peak metamorphic conditions. This interpretation is consistent with the stability of the observed (cordierite-absent) peak mineral assemblage occurring at higher pressure.

In sample 6251, measured X_{Fe} and X_{gr} compositions in garnet suggest that peak metamorphic conditions were ~ 850–950°C and 5.4–6.6 kbar. However, these P–T conditions correspond to garnet–cordierite–spinel-bearing and/or garnet–sillimanite–cordierite-bearing assemblages. This is inconsistent with the inference that the observed spinel and sillimanite do not form part of the peak mineral assemblage. Spinel is present as a minor phase ($\sim 1\%$ abundance) and always occurs as inclusions within garnet or hosted within cordierite that is inferred to have replaced former peak metamorphic garnet grains. Therefore, spinel is interpreted to have potentially formed part of the prograde mineral assemblage. However, as this study does not account for the possibility that the rocks of the HJA underwent melt loss through melt reintegration modelling (e.g. Korhonen *et al.* 2010, Anderson *et al.* 2013), the presence or absence of spinel cannot be used reliably to make inferences about the prograde P–T path. Furthermore, electron microprobe mineral chemistry indicates that spinel contains a moderate amount of ZnO (0.97–1.17 wt%; Tables III & S1). Components such as zinc are known to enhance spinel stability to lower temperatures and higher pressures (e.g. Nichols *et al.* 1992, Tajčmanová *et al.* 2009). However, the current absence of thermodynamic models for Zn-bearing solid solutions limits the phase equilibria modelling approach because this P–T shift cannot be effectively quantified. Thus, the presence or absence of spinel cannot be reliably used as a constraint on the P–T conditions for this sample.

Although sillimanite is not interpreted to be part of the peak metamorphic assemblage, the calculated abundance of sillimanite is relatively low within the P–T region estimated from compositional isopleths (~ 1–2% abundance). Therefore, at these conditions, any peak sillimanite would probably not be readily observed in a thin section. Sillimanite does occur as rare inclusions within garnet, but not as a noticeable matrix phase. This microstructural relationship is suggestive that sillimanite grew as part of an earlier and probably higher pressure, prograde assemblage, and therefore, supports the notion that this sample evolved along a broadly clockwise P–T

evolution. However, as for spinel, the presence of sillimanite cannot be used to definitively constrain the absolute prograde P–T trajectory for this sample.

The new P–T determinations presented in this study suggest that overall the HJA attained slightly higher temperature and pressure conditions than previously obtained by Stüwe & Powell (1989). Previous P–T estimates constrained using conventional thermobarometry were ~750–800°C at 5–6 kbar for the Bunger Hills and ~700–750°C at 7–9 kbar for the HJA (Stüwe & Powell 1989, Sheraton et al. 1995). The slightly higher pressure conditions proposed for the HJA compared with the Bunger Hills are consistent with the observation of garnet in mafic granulite in the north-eastern HJA (Sheraton et al. 1995). However, the previous constraint on peak temperature for the HJA is likely to be unreliable as the garnet utilized for those P–T calculations occurred as a coronae about orthopyroxene and was accordingly interpreted to have been of retrograde origin (Sheraton et al. 1995). The P–T calculations done using conventional thermobarometry rely heavily upon individual, measured mineral compositions, which, as in this example, may not be truly indicative of the compositions that were formed at the peak of metamorphism if the minerals underwent diffusion as is typical at granulite facies.

Stüwe & Powell (1989) initially proposed that rocks of the Bunger Hills underwent an anticlockwise P–T evolution. This assertion was made on the basis that relict spinel was commonly surrounded by a cordierite, garnet and/or sillimanite coronae which ostensibly reflected the reaction between a formerly more widespread, low pressure (~800°C, 4 kbar) spinel–quartz-bearing assemblage to produce a higher pressure, garnet–sillimanite–cordierite-bearing assemblage (~750°C, 6–7 kbar; Stüwe & Powell 1989). However, Sheraton et al. (1995) observed in some metapelitic rocks that spinel and quartz commonly formed a stable relationship, often occurring in contact with one another. Although only volumetrically minor (~1% abundance), Sheraton et al. (1995) also noted the pervasiveness of spinel throughout the metapelitic rocks and thus question the validity of the notion of subsequent overprinting by a high pressure assemblage. Furthermore, the significance of spinel on P–T determinations relies heavily on its ZnO content; as the Zn content in spinel is unreported by previous workers, earlier interpretations on the metamorphic evolution made on the basis of the presence of spinel cannot be considered overly robust.

Cordierite is present in samples 6264 and 6251. Typically, cordierite occurs adjacent to and bridges anhedral garnet grains (e.g. Fig. 2a & b) and sometimes completely isolates relict garnet grains (e.g. Fig. 2f). Cordierite occurring near garnet also commonly hosts sillimanite in sample 6264 (e.g. Fig. 2b & c). Sillimanite is also often included within garnet, but garnet never hosts cordierite. Therefore, the spatial relationship between garnet and cordierite (and sillimanite in sample 6264) suggests that the abundance of cordierite increased following the growth of garnet and sillimanite at the inferred peak metamorphic conditions. Decreasing garnet and sillimanite modal abundance and increasing cordierite modal abundance occurs along a down-pressure, down-temperature trajectory (e.g. Fig. S3). Furthermore, rare cordierite–quartz symplectites also occur adjacent to garnet (e.g. Fig. 3). Previous studies have ascribed cordierite–quartz symplectites to garnet breakdown and/or the melt assisted breakdown of feldspar in the presence of a Fe–Mg phase (Henry 1974, Mohan & Windley 1993, Nandakumar & Harley 2000); however, the occurrence of these intergrowths typically adjacent to garnet in this instance is suggestive of the former interpretation. In this study, evidence for cordierite growth after garnet in samples 6264 and 6251, and rare growth of ilmenite about rutile, suggests that, in contrast to the initial interpretations of Stüwe & Powell (1989), the rocks of the HJA record evidence for a clockwise (decompressional) P–T path. The absence of magnetite in sample 6251 further suggests that the trajectory of this down-temperature P–T path may have been relatively shallow. This conclusion is supported by another sample of metapelite located north of Raketa Island (sample 86286263) reported by Sheraton et al. (1995) to show garnet partially replaced by orthopyroxene–cordierite–plagioclase symplectites, a microstructural relationship that has been previously ascribed to a decompressional P–T evolution (e.g. Brandt et al. 2003, Tong et al. 2014). Sheraton et al. (1995) also report on garnet occurring as symplectitic rims about orthopyroxene in granite from the Paz Cove batholith and orthogneiss from the north-east HJA (sample 86285979), inferred to have developed as a result of near-isobaric cooling.

Re-examination of the HJA P–T conditions in this study suggests that the metamorphic evolution of these rocks is incompatible with the tectonic model proposed initially by Stüwe & Powell (1989) involving extension followed by compressional deformation, although Harris (1995) note that this initial interpretation was also subsequently re-evaluated. If the rocks underwent thickening post-extension then an anticlockwise P–T path would be expected (e.g. Brown 1993). In contrast, the retrograde evolution of the HJA presented here is characterized by a pressure decrease during cooling from a metamorphic peak that occurred at a high temperature and medium pressure. This scenario appears more consistent with the notion of thinning of over-thickened crust. However, there is also currently little documented structural evidence for extensional thinning in the Bunger Hills and HJA, and, therefore, the drivers for

metamorphism and the down-pressure retrograde evolution proposed in this study remain unclear.

A two-stage tectonothermal history has been proposed for the Windmill Islands involving upper amphibolite facies metamorphism (> 750°C, 4 kbar) at *c.* 1340–1300 Ma, and subsequently granulite facies metamorphism (~ 850–900°C, 5–7 kbar) at *c.* 1240–1140 Ma (Post 2000). The latter phase, coincident with Stage 2 of the Albany–Fraser Orogeny and high temperature metamorphism in the HJA, is inferred to have involved a post-peak clockwise P–T–time path, interpreted to reflect exhumation and unloading of the terrane following crustal thickening during continental collision (Post 2000). Similarly, peak granulite facies metamorphism (800°C, > 5 kbar) is also recorded by the Salisbury Gneiss in the Nornalup Complex at *c.* 1214 ± 8 Ma with zircon rims dating to 1182 ± 13 Ma, suggestive of decompression from peak metamorphic conditions by exhumation along thrust zones (Clark *et al.* 2000). Although peak metamorphism of the HJA occurred during Stage 2 of the Albany–Fraser Orogeny, the P–T conditions attained are also similar to those recorded at *c.* 1290 Ma by the Fraser Zone within south-western Australia (~ 850°C and 7–9 kbar; Clark *et al.* 2014). These rocks are interpreted to reflect the mid-crustal emplacement of mafic magmatism into a back-arc environment followed by near-isobaric cooling at depth (~ 9 kbar, ~ 27 km depth; Clark *et al.* 2014). A similar scenario for the HJA would justify the elevated temperatures and medium pressures attained during peak metamorphism but does not necessarily explain the inferred clockwise P–T evolution. Geochronological data from the Bunger Hills currently suggests that magmatism also occurred following the main phase of metamorphism (Sheraton *et al.* 1992).

Conclusions

Legacy thin section samples provide a valuable record of the geological characteristics of rocks of the HJA that are located in a pivotal yet largely inaccessible part of the MAFO. Metasedimentary rocks from the HJA suggest that this region underwent granulite facies metamorphism (~ 850–950°C and 6–9 kbar) at *c.* 1183 Ma. The inferred growth of cordierite after garnet further suggests that these rocks cooled along a decompressional P–T trajectory following peak metamorphic conditions. The timing of metamorphism determined in this study confirms the age previously constrained for the Bunger Hills–HJA region. However, the new P–T determinations suggest that peak metamorphic conditions within the HJA attained slightly higher temperatures and pressures than previously proposed. In contrast to the initial interpretations from reconnaissance P–T work, the results of this study also suggest that the rocks evolved along a clockwise rather than anticlockwise P–T path.

Author contribution statement

NMT was primarily responsible for data collection, data analysis and preparation of the manuscript. Both authors were involved in the original paper concept and design, and subsequent drafting and revision of the manuscript.

Supplemental material

Three supplemental figures and a table will be found at http://dx.doi.org/10.1017/S095410201600033X.

References

AITKEN, A.R.A. & BETTS, P.G. 2008. High-resolution aeromagnetic data over central Australia assist Grenville-era (1300–1100 Ma) Rodinia reconstructions. *Geophysical Research Letters*, **35**, 10.1029/2007 GL031563.

ANDERSON, J.R., KELSEY, D.E., HAND, M. & COLLINS, W.J. 2013. Conductively driven, high-thermal gradient metamorphism in the Anmatjira Range, Arunta region, central Australia. *Journal of Metamorphic Geology*, **31**, 1003–1026.

BETTS, P.G. & GILES, D. 2006. The 1800–1100 Ma tectonic evolution of Australia. *Precambrian Research*, **144**, 92–125.

BODORKOS, S. & CLARK, D.J. 2004. Evolution of a crustal-scale transpressive shear zone in the Albany–Fraser Orogen, SW Australia: 2. Tectonic history of the Coramup Gneiss and a kinematic framework for Mesoproterozoic collision of the West Australian and Mawson cratons. *Journal of Metamorphic Geology*, **22**, 713–731.

BOGER, S.D. 2011. Antarctica – before and after Gondwana. *Gondwana Research*, **19**, 335–371.

BRANDT, S., KLEMD, R. & OKRUSCH, M. 2003. Ultrahigh-temperature metamorphism and multistage evolution of garnet–orthopyroxene granulites from the Proterozoic Epupa Complex, NW Namibia. *Journal of Petrology*, **44**, 1121–1144.

BROWN, M. 1993. P-T-T evolution of orogenic belts and the causes of regional metamorphism. *Journal of the Geological Society*, **150**, 227–241.

CADDICK, M.J., KONOPÁSEK, J. & THOMPSON, A.B. 2010. Preservation of garnet growth zoning and the duration of prograde metamorphism. *Journal of Petrology*, **51**, 2327–2347.

CAWOOD, P.A. & KORSCH, R.J. 2008. Assembling Australia: Proterozoic building of a continent. *Precambrian Research*, **166**, 1–38.

CLARK, C., KIRKLAND, C.L., SPAGGIARI, C.V., OORSCHOT, C., WINGATE, M.T.D. & TAYLOR, R.J. 2014. Proterozoic granulite formation driven by mafic magmatism: an example from the Fraser Range Metamorphics, Western Australia. *Precambrian Research*, **240**, 1–21.

CLARK, D.J., HENSEN, B.J. & KINNY, P.D. 2000. Geochronological constraints for a two-stage history of the Albany–Fraser Orogen, Western Australia. *Precambrian Research*, **102**, 155–183.

CLARKE, G.L., SUN, S.S. & WHITE, R.W. 1995. Grenville-age belts and associated older terranes in Australia and Antarctic. *AGSO Journal of Australian Geology & Geophysics*, **16**, 25–39.

DING, P. & JAMES, P. 1991. Structural evolution of the Bunger Hills area of East Antarctic. *In* THOMSON, M.R.A., CRAME, J.A. & THOMSON, J.W., *eds. Geological evolution of Antarctic*. Cambridge: Cambridge University Press, 13–18.

DROOP, G.T.R. 1987. A general equation for estimating Fe^{3+} concentrations in ferromagnesian silicates and oxides from microprobe analyses, using stoichiometric criteria. *Mineralogical magazine*, **51**, 431–435.

DUEBENDORFER, E.M. 2002. Regional correlation of Mesoproterozoic structures and deformational events in the Albany–Fraser orogen, Western Australia. *Precambrian Research*, **116**, 129–154.

FITZSIMONS, I.C.W. 2000. Grenville-age basement provinces in East Antarctica: evidence for three separate collisional orogens. *Geology*, **28**, 879–882.

FITZSIMONS, I.C.W. 2003. Proterozoic basement provinces of southern and southwestern Australia, and their correlation with Antarctic. *Special Publication of the Geological Society of London*, No. 206, 93–130.

GRIFFIN, W.L., POWELL, W.J., PEARSON, N.J. & O'REILLY, S.Y. 2008. GLITTER: data reduction software for laser ablation ICP–MS. *In* SYLVESTER, P., *ed. Laser ablation ICP–MS in the earth sciences: current practices and outstanding issues*. Vancouver: Mineralogical Association of Canada, 204–207.

HARRIS, L.B. 1995. Correlations between the Albany, Fraser and Darling mobile belts of Western Australia and Mirnyy to Windmill Islands in the East Antarctic Shield: implications for Proterozoic Gondwanaland reconstructions. *Memoirs - Geological Society of India*, 47–72.

HENRY, J. 1974. Garnet-cordierite gneisses near the Egersund-Ogna anorthositic intrusion, southwestern Norway. *Lithos*, **7**, 207–216.

HOLLAND, T.J.B. & POWELL, R. 1998. An internally consistent thermodynamic data set for phases of petrological interest. *Journal of metamorphic Geology*, **16**, 309–343.

HOLLAND, T.J.B. & POWELL, R. 2011. An improved and extended internally consistent thermodynamic dataset for phases of petrological interest, involving a new equation of state for solids. *Journal of Metamorphic Geology*, **29**, 333–383.

HOWARD, H.M., SMITHIES, R.H., KIRKLAND, C.L., KELSEY, D.E., AITKEN, A., WINGATE, M.T.D., DE GROMARD, R.Q., SPAGGIARI, C.V. & MAIER, W.D. 2015. The burning heart – the proterozoic geology and geological evolution of the west Musgrave Region, Central Australia. *Gondwana Research*, **27**, 64–94. Erratum: *Gondwana Research*, **28**, 1255.

KELSEY, D.E. & HAND, M. 2015. On ultrahigh temperature crustal metamorphism: phase equilibria, trace element thermometry, bulk composition, heat sources, timescales and tectonic settings. *Geoscience Frontiers*, **6**, 311–356.

KIRKLAND, C.L., SMITHIES, R.H. & SPAGGIARI, C.V. 2015. Foreign contemporaries – unravelling disparate isotopic signatures from Mesoproterozoic Central and Western Australia. *Precambrian Research*, **265**, 218–231.

KIRKLAND, C.L., SMITHIES, R.H., WOODHOUSE, A.J., HOWARD, H.M., WINGATE, M.T.D., BELOUSOVA, E.A., CLIFF, J.B., MURPHY, R.C. & SPAGGIARI, C.V. 2013. Constraints and deception in the isotopic record: the crustal evolution of the west Musgrave Province, central Australia. *Gondwana Research*, **23**, 759–781.

KIRKLAND, C.L., SPAGGIARI, C.V., PAWLEY, M.J., WINGATE, M.T.D., SMITHIES, R.H., HOWARD, H.M., TYLER, I.M., BELOUSOVA, E.A. & POUJOL, M. 2011. On the edge: U-Pb, Lu-Hf, and Sm-Nd data suggests reworking of the Yilgarn craton margin during formation of the Albany-Fraser Orogen. *Precambrian Research*, **187**, 223–247.

KORHONEN, F.J., SAITO, S., BROWN, M. & SIDDOWAY, C.S. 2010. Modeling multiple melt loss events in the evolution of an active continental margin. *Lithos*, **116**, 230–248.

MOHAN, A. & WINDLEY, B.F. 1993. Crustal trajectory of sapphirine-bearing granulites from Ganguvarpatti, South India: evidence for an isothermal decompression path. *Journal of Metamorphic Geology*, **11**, 867–878.

NANDAKUMAR, V. & HARLEY, S.L. 2000. A reappraisal of the pressure-temperature path of granulites from the Kerala Khondalite Belt. *Journal of Geology*, **108**, 687–703.

NELSON, D.R., MYERS, J.S. & NUTMAN, A.P. 1995. Chronology and evolution of the Middle Proterozoic Albany-Fraser Orogen, Western Australia. *Australian Journal of Earth Sciences*, **42**, 481–495.

NICHOLS, G.T., BERRY, R.F. & GREEN, D.H. 1992. Internally consistent gahnitic spinel-cordierite-garnet equilibria in the FMASHZn system – geothermobarometry and applications. *Contributions to Mineralogy and Petrology*, **111**, 362–377.

PAYNE, J.L., HAND, M., BAROVICH, K.M. & WADE, B.P. 2008. Temporal constraints on the timing of high-grade metamorphism in the northern Gawler Craton: implications for assembly of the Australian Proterozoic. *Australian Journal of Earth Sciences*, **55**, 623–640.

PEARCE, M.A., WHITE, A.J.R. & GAZLEY, M.F. 2015. TCInvestigator: automated calculation of mineral mode and composition contours for thermocalc pseudosections. *Journal of Metamorphic Geology*, **33**, 413–425.

POST, N.J. 2000. *Unravelling Gondwana fragments: an integrated structural, isotopic and petrographic investigation of the Windmill Islands, Antarctica*. PhD thesis, University of New South Wales, 382 pp. [Unpublished].

RAVICH, M.G.E., KLIMOV, L. & SOLOV'EV, D. 1968. *The Pre-Cambrian of East Antarctica*. Jerusalem: Israel Program for Scientific Translations, 475 pp.

SHERATON, J.W., BLACK, L.P. & TINDLE, A.G. 1992. Petrogenesis of plutonic rocks in a Proterozoic granulite-facies terrane – the Bunger Hills, East Antarctica. *Chemical Geology*, **97**, 163–198.

SHERATON, J.W., BLACK, L.P., McCULLOCH, M.T. & OLIVER, R.L. 1990. Age and origin of a compositionally varied mafic dyke swarm in the Bunger Hills, East Antarctica. *Chemical Geology*, **85**, 215–246.

SHERATON, J.W., TINGEY, R.J., BLACK, L.P. & OLIVER, R.L. 1993. Geology of the Bunger Hills area, Antarctica: implications for Gondwana correlations. *Antarctica Science*, 5, 85–102.

SHERATON, J.W., TINGEY, R.J., OLIVER, R.L. & BLACK, L.P. 1995. Geology of the Bunger Hills-Denman Glacier region, East Antarctic. *AGSO Bulletin*, No. 244, 1–136.

SMITHIES, R.H., HOWARD, H.M., EVINS, P.M., KIRKLAND, C.L., KELSEY, D.E., HAND, M., WINGATE, M.T.D., COLLINS, A.S. & BELOUSOVA, E. 2011. High-temperature granite magmatism, crust-mantle interaction and the Mesoproterozoic intracontinental evolution of the Musgrave Province, Central Australia. *Journal of Petrology*, **52**, 931–958.

SMITHIES, R.H., KIRKLAND, C.L., KORHONEN, F.J., AITKEN, A.R.A., HOWARD, H.M., MAIER, W.D., WINGATE, M.T.D., DE GROMARD, R.Q. & GESSNER, K. 2015. The Mesoproterozoic thermal evolution of the Musgrave Province in central Australia – plume vs. the geological record. *Gondwana Research*, **27**, 1419–1429.

SMITS, R.G., COLLINS, W.J., HAND, M., DUTCH, R. & PAYNE, J. 2014. A Proterozoic Wilson cycle identified by Hf isotopes in central Australia: implications for the assembly of Proterozoic Australia and Rodinia. *Geology*, **42**, 231–234.

SPAGGIARI, C.V. & TYLER, I.M. 2014. *Albany-Fraser Orogen seismic and magnetotelluric (MT) workshop 2014: extended abstracts*. Record 2014/6. East Perth: Geological Survey of Western Australia, 182 pp.

SPAGGIARI, C.V., KIRKLAND, C.L., SMITHIES, R.H., WINGATE, M.T.D. & BELOUSOVA, E.A. 2015. Transformation of an Archean craton margin during Proterozoic basin formation and magmatism: the Albany–Fraser Orogen, Western Australia. *Precambrian Research*, **266**, 440–466.

SPEAR, F.S. 1991. On the interpretation of peak metamorphic temperatures in light of garnet diffusion during cooling. *Journal of Metamorphic Geology*, **9**, 379–388.

STÜWE, K. & POWELL, R. 1989. Metamorphic evolution of the Bunger Hills, East Antarctica: evidence for substantial post-metamorphic peak compression with minimal cooling in a Proterozoic orogenic event. *Journal of Metamorphic Geology*, **7**, 449–464.

STÜWE, K. & WILSON, C.J.L. 1990. Interaction between deformation and charnockite emplacement in the Bunger Hills, East Antarctica. *Journal of Structural Geology*, **12**, 767–783.

TAJČMANOVÁ, L., KONOPÁSEK, J. & KOŠLER, J. 2009. Distribution of zinc and its role in the stabilization of spinel in high-grade felsic rocks of the Moldanubian domain (Bohemian Massif). *European Journal of Mineralogy*, **21**, 407–418.

TONG, L.X., LIU, X.H., WANG, Y.B. & LIANG, X.R. 2014. Metamorphic P-T paths of metapelitic granulites from the Larsemann Hills, East Antarctica. *Lithos*, **192**, 102–115.

TUCKER, N.M., HAND, M., KELSEY, D.E. & DUTCH, R.A. 2015. A duality of timescales: short-lived ultrahigh temperature metamorphism preserving a long-lived monazite growth history in the Grenvillian Musgrave–Albany–Fraser Orogen. *Precambrian Research*, **264**, 204–234.

WALSH, A.K., KELSEY, D.E., KIRKLAND, C.L., HAND, M., SMITHIES, R.H., CLARK, C. & HOWARD, H.M. 2015. P–T–t evolution of a large, long-lived, ultrahigh-temperature Grenvillian belt in central Australia. *Gondwana Research*, **28**, 531–564.

WHITE, L.T., GIBSON, G.M. & LISTER, G.S. 2013. A reassessment of paleogeographic reconstructions of eastern Gondwana: bringing geology back into the equation. *Gondwana Research*, **24**, 984–998.

WHITE, R.W., POWELL, R., HOLLAND, T.J.B., JOHNSON, T.E. & GREEN, E.C.R. 2014. New mineral activity–composition relations for thermodynamic calculations in metapelitic systems. *Journal of Metamorphic Geology*, **32**, 261–286.

ZHANG, S.H., ZHAO, Y., LIU, X.C., LIU, Y.S., HOU, K.J., LI, C.F. & YE, H. 2012. U-Pb geochronology and geochemistry of the bedrocks and moraine sediments from the Windmill Islands: implications for Proterozoic evolution of East Antarctica. *Precambrian Research*, **206**, 52–71.